ACS OMEGA

http://pubs.acs.org/journal/acsodf

Article

Molecular-Level Insights into the Reaction Mechanisms of Reductive Etherification for the Production of Synthetic Biofuels

Hieu A. Doan,[∇] Chenyang Li,[∇] Jacob H. Miller,* Nicole J. LiBretto, Alexander L. Rein, Mingxia Zhou, Glenn R. Hafenstine, Derek R. Vardon, Susan E. Habas, and Rajeev S. Assary*

Cite This: *ACS Omega* 2025, 10, 16472−16480

Read Online

ACCESS | Metrics & More | Article Recommendations | Supporting Information

ABSTRACT: Reductive etherification provides a pathway for creating low-carbon-intensity distillate fuel blendstocks and chemicals from biomass-derived alcohols and ketones. In this work, we examine the reductive etherification of representative model compounds, *n*-butanol and 4-heptanone, to form 4-butoxyheptane over size-controlled Pd nanoparticles supported on $NbOPO_4$ through a combination of experiments and density functional theory (DFT) calculations. Reaction rate and selectivity trends from packed-bed reactions show that both the catalyst and support are needed to carry out the reaction and that reaction rates increase with increasing Pd particle size. The DFT calculations show that the reaction most likely proceeds via the formation of an enol intermediate on the support, which is subsequently hydrogenated on Pd. Furthermore, we rationalize the dependence of 4-butoxyheptane formation rates on Pd particle size by showing the energetic favorability of enol ether hydrogenation on low-index terrace sites (Pd(111) and (100)) compared to that on high-index step sites (Pd(110)).

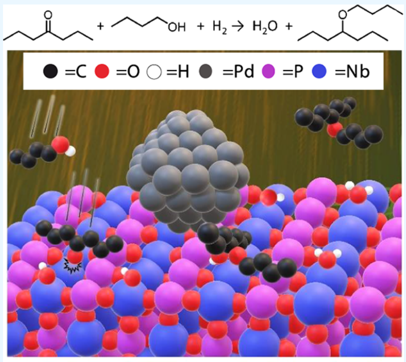

1. INTRODUCTION

Synthetic chemical pathways are critical for producing biomass-derived fuels to decarbonize heavy-duty transportation.[1] Branched ethers formed from biomass upgrading offer the advantageous fuel properties of low-sooting potential and high cetane number, making them suitable as distillate or diesel blendstocks.[2] Reductive etherification, which produces branched ether molecules from the coupling of ketones and alcohols, is a promising catalytic process for producing such molecules. The ketone and alcohol reactants for reductive etherification can be produced from biomass through methods such as waste sugar fermentation,[3] catalytic carbohydrate upgrading,[4,5] and conversion of wet-waste-derived volatile fatty acids (VFAs).[6] The VFA pathway is of particular interest, as the upgrading of these intermediates to liquid transportation fuels was recently shown by Huq et al. to have net-negative life-cycle carbon intensity (−55 g CO_2 eq/MJ) and promising economic prospects.[7] Reductive etherification chemistry has the flexibility to upgrade alcohols and ketones into ether bioblendstocks and could lower separation costs and increase overall process carbon yields compared to other carboxylic acid upgrading processes.[4,8,9]

Hafenstine et al.[4] recently performed reductive etherification over Pd nanoparticles supported on several metal oxides, including Nb_2O_5, $NbOPO_4$, and TiO_2. The Pd/$NbOPO_4$ catalyst exhibited the highest rates and selectivity for *n*-butanol and 4-heptanone reductive etherification to 4-butoxyheptane, or 4-BH. Further economization of 4-BH production is key to demonstrating the value of the pathway and can be achieved via catalyst optimization. First, maximizing rates of 4-BH production is critical for reducing the required catalyst amounts and reactor sizes.[4] Second, since the cost of noble metal-promoted catalysts, such as Pd/$NbOPO_4$, is also driven by metal content, formulating catalysts that achieve high rates with minimal noble metal content is crucial. We note that there have been recent experimental mechanistic studies of reductive etherification over non-noble metal catalysts[10−12] (e.g., oxide-supported cobalt and copper[13]), but Pd/$NbOPO_4$ exhibits superior rates and selectivity.

Catalyst optimization can also be achieved through an enhanced understanding of reaction mechanisms, especially for multifunctional catalysts such as those utilized in this work. Reductive etherification is known to proceed over metal nanoparticles supported on oxides, but the specific mechanistic roles of either material have yet to be fully elucidated.[14,15] Furthermore, Garcia-Ortiz et al.[16] and Bethmont et al.[17] observed that reductive etherification rates increased with increasing crystallite size on Pd-based catalysts (from 5 to 10 or 10−18 nm, respectively), but the fundamental reasons behind this increase are not entirely understood.

Received: December 4, 2024
Revised: March 20, 2025
Accepted: March 27, 2025
Published: April 16, 2025

https://doi.org/10.1021/acsomega.4c09698

We herein use density functional theory (DFT)-based atomistic simulations to validate experimental measurements of catalytic rates and selectivity of the reductive etherification reaction over size-controlled Pd nanoparticles supported on $NbOPO_4$ to fill the gap between experimental observations and molecular-level insights. First, we demonstrate through experimental observations in packed-bed reactors that reductive etherification requires both acid and metal surfaces and that rates increase with increasing Pd particle size. We then justify these experimental observations through DFT simulations of reductive etherification over Pd/$NbOPO_4$. We determine the reaction energetics of three etherification pathways (direct, ketal, and enol) and identify the most energetically favorable pathway, which involves enol formation on $NbOPO_4$(100) followed by hydrogenation on Pd(111). Finally, we rationalize the experimental observation of increasing etherification rates with increasing particle size by showing that hydrogenation is more energetically favorable on Pd(111) and Pd(100), two facets that dominate larger nanoparticles, than on Pd(110), a facet relevant to smaller particles.

2. METHODS

2.1. Experimental Methods. *2.1.1. Catalyst Synthesis.* Size-controlled Pd nanoparticles on $NbOPO_4$ were prepared by incipient wetness impregnation based on approaches demonstrated in the literature.[18] Tetraamminepalladium(II) nitrate solution (10 wt % in water, Sigma-Aldrich) was added dropwise to 5 g of $NbOPO_4$ until the incipient wetness point was reached. The material was dried in an oven at 50 °C to remove water. Additional tetraamminepalladium(II) nitrate solution was added to the material to reach a target Pd loading of 3.5 wt %. The resulting material was dried at room temperature for 2 h and then overnight at 125 °C. After drying, the material was divided into three batches and calcined at 200, 400, and 600 °C, respectively, for 3 h. Each material was thermally reduced in 5% H_2 by heating at 2 °C/min to 250 °C and holding this temperature for 2 h. After being cooled to room temperature, the catalysts were passivated in 1% aqueous O_2/N_2 before being removed from the furnace.

2.1.2. Inductively Coupled Plasma Optical Emission Spectroscopy (ICP-OES). The Pd content of the Pd/$NbOPO_4$ samples was determined using inductively coupled plasma optical emission spectroscopy (ICP-OES), performed by Galbraith Laboratories (Knoxville, TN).

2.1.3. X-ray Diffraction (XRD). Powder XRD data were collected using a Rigaku Ultima IV diffractometer with a Cu Kα source (40 kV, 44 mA). Diffraction patterns were collected in the 2θ range of 20−100° at a scan rate of 40°/min. The Pd/$NbOPO_4$ catalysts were supported on a glass sample holder with a 0.5 mm recessed sample area and were pressed into the recess with a glass slide to obtain a uniform z-axis height. A NIST Si standard was used to calibrate the XRD peak positions. Theoretical diffraction patterns were simulated at room temperature using crystal information files (cif) downloaded from the Inorganic Crystal Structure Database (ICSD) and imported into the Materials Analysis Using Diffraction (MAUD) program to identify the catalyst phase.

2.1.4. Transmission Electron Microscopy (TEM). Samples for TEM analysis were drop-cast onto lacey carbon-coated Cu mesh grids (Ted Pella, part no. 01895-F) from ethanol suspensions. Imaging was performed using an FEI Tecnai G2 ST30 TEM operated at 200 kV, and all image analysis was conducted with ImageJ software.[19] The Pd particle diameter distributions were determined from manual diameter measurements of >100 particles.

2.1.5. CO Chemisorption. Pulse CO chemisorption was performed using an Altamira instrument on Pd/$NbOPO_4$ materials. Prior to analysis, each material was reduced in H_2 by heating at 2 °C/min to 200 °C and holding for 2 h. The reactor was then cooled to 40 °C and purged with He. Pulse CO chemisorption was performed at 40 °C.

2.1.6. Reductive Etherification Reaction Testing. A 50%/50% (mol/mol) mixture of 4-heptanone (Sigma-Aldrich, 98%) and 1-butanol (Sigma-Aldrich, 99.8%) was fed using an HPLC pump (Chromtech) along with H_2 (ultrahigh purity, 99.999+%, Matheson) controlled by a mass flow controller (Brooks Instruments) to a trickle-bed reactor described previously.[4] Reactions occurred in a 0.5 in. OD Dursan-coated stainless-steel tube heated by a clamshell furnace (Carbolite Gero). Reactions were performed at 200 °C, and the temperature was monitored with a dual thermocouple (Omega) embedded in the catalyst bed. A pressure of 70 bar was maintained by using a backpressure regulator (Brooks Instruments). Catalyst beds consisted of 200 mg of Pd/$NbOPO_4$ or $NbOPO_4$ powder mixed with 1.8 g of quartz sand secured between two plugs of glass wool; the remaining volume of the reactor tube was filled with glass beads (BioSpec Products). The liquid mixture was fed at 0.05 mL min^{-1} and H_2 was fed at 30 sccm, with flows increased 10-fold during the first 15 min of reactor operation to accelerate initial transient behavior. The reactor effluent was passed through a condenser operating at 2 °C, and the resultant liquids were captured in a knockout pot (Parr), from which they were periodically collected. Product liquids were weighed and compared with mass changes in the HPLC pump feed bottle, which was stored on a mass balance (Mettler Toledo). Liquid sample analysis was performed using a GC/MS (Agilent 7890*A*/5975C) with an attached methanizer-FID (PolyARC).

Kinetic data were measured after 16 h of reaction to study reactivity after the initial transient behavior. Carbon balances at this time were usually closed between 90 and 110%. Carbon conversion (X) for each liquid sample was defined as:

$$X = \frac{\sum_{i=\text{products}} N_{C,i} n_i}{4n_{\text{butanol},0} + 7n_{\text{heptanone},0}} \quad (1)$$

Here, $N_{C,i}$ is the carbon number of product i, n_i is the collected moles of product i in a sample, and $n_{\text{butanol},0}$ and $n_{\text{heptanone},0}$ are the moles of butanol and heptanone fed during each sample collection interval. Carbon conversion was 15% or less after 16 h on stream; this was considered differential. The rates of 4-BH production (r) were quantified using eq 2:

$$r = \frac{n_{4\text{-BH}}}{m_{\text{Pd/NbOPO}_4} t_{\text{sample}}} \quad (2)$$

In eq 2, t_{sample} is the time duration during which the liquid from a sample is collected in the knockout pot. The reported rates are averages of 3−4 measurements taken between 16 and 26 h on stream. The variation of reductive etherification rates with the Pd particle size discussed herein implies that the observed rates are kinetically controlled and not influenced by significant heat or mass transport gradients. We also tracked the carbon selectivity of all products (S_i) in each collected sample:

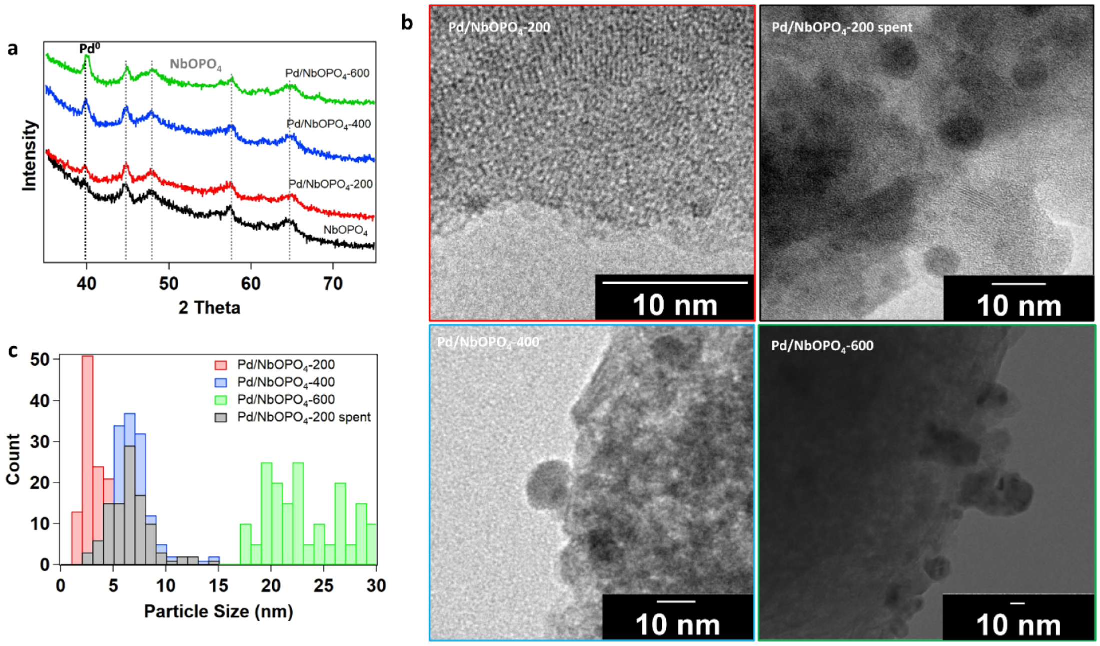

Figure 1. (a) Particle diameter distributions of Pd/$NbOPO_4$ catalysts with increasing calcination temperatures, (b) representative TEM images of selected catalysts, and c) XRD patterns of Pd/$NbOPO_4$ catalysts with increasing calcination temperatures. Pd(111) reflection is indicated by a vertical black dashed line (39.9°), and major $NbOPO_4$ reflections are indicated by vertical gray dashed lines (2θ = 44.1°, 47.0°, 56.7°, 62.8°).

$$S_i = \frac{N_{C,i} n_i}{\sum_{j=\text{products}} N_{C,j} n_j} \tag{3}$$

2.2. Computational Methods.

Density functional theory (DFT)[20] calculations were performed using the Vienna Ab initio simulation package (VASP)[21] with accurate precision and spin polarization. The core and valence electrons were represented by the projected augmented wave (PAW)[22] method with a kinetic energy cutoff of 400 eV. Exchange and correlation were described by the generalized gradient approximation (GGA) Perdew−Burke−Ernzerhof (PBE) functional with van der Waals corrections.[23,24] Second-order Methfessel−Paxton[25] smearing with a Fermi temperature of k_BT = 0.2 eV was employed, and the total energies were subsequently extrapolated to k_BT = 0 eV. The self-consistent iterations were converged to 1×10^{-4} eV per cell ($<1 \times 10^{-6}$ eV per atom). For geometry optimizations, forces on unconstrained atoms were converged to below 0.05 eV/Å. The climbing image nudged elastic band (CI-NEB) method was used to calculate the activation energies, and the calculations were sufficiently converged when the maximum force component perpendicular to the reaction path was below 0.05 eV/Å.

The $NbOPO_4$(100) and Pd(111) surfaces were modeled as slabs with (3 × 4) and (6 × 6) supercells, respectively. Each surface consisted of an equivalent of three layers, where the top two layers were allowed to relax, and the bottom layer was fixed to the bulk atomic positions. A vacuum of 20 Å was added above the slabs in the direction perpendicular to the surface. The Brillouin zone was sampled using generalized Monkhorst−Pack grids generated by the *k*-point server,[26,27] with a minimum distance of 47 Å between lattice points on the corresponding real-space lattice.

The binding energy (BE) of an intermediate with the catalyst surface slab was computed as

$$\mathrm{BE}_{X^*} = E(\text{slab} + \text{adsorbed } X^*) - E(\text{slab}) - E(X(\text{g})) \tag{4}$$

where E(slab + adsorbed X*) is the energy of the total system consisting of the catalyst surface slab and the adsorbed species, E(slab) is the energy of the clean slab, and $E(X(\text{g}))$ is the gas-phase energy. The vibrational frequencies and zero-point energies were computed for estimating the thermodynamic properties (Gibbs free energy). For example, the reference state of the Gibbs free energy of H_2(g) under experimental conditions was calculated as:

$$G(T, p) = E_{\text{DFT}} + E_{\text{ZPE}} + \int_0^T C_p dT - TS^T + k_BT\ln\left(\frac{p}{p^o}\right) \tag{5}$$

where E_{DFT} is the DFT-computed total energy, E_{ZPE} is the zero-point energy correction, T is 200 °C, and p is 1000 psig.

3. RESULTS AND DISCUSSION

3.1. Reductive Etherification on Size-Controlled Pd Nanoparticles.

Our previous work developed a Pd/$NbOPO_4$ catalyst with high (>80%) reductive etherification selectivity.[4] The mean Pd particle size of this catalyst was 10 nm; however, the wide particle size distribution (standard deviation of 9 nm) limited the ability to determine the effect of particle size on the reaction rate. Thus, any effect of metal particle size on reductive etherification rates, such as the increases in rates with increasing particle size observed by Garcia-Ortiz et al.[16] and Bethmont et al.[17], was not discernible. We synthesized several Pd/$NbOPO_4$ materials with narrow particle size distributions to observe the effects of Pd crystallite size on reductive etherification rates and selectivity. Pd was deposited on the support using a standard incipient wetness impregnation methodology, and variation in the calcination temperature (prior to reduction) was used to control the resulting particle sizes. The materials were termed Pd/NbOPO$_4$-200, Pd/NbOPO$_4$-400, and Pd/NbOPO$_4$-600, representing calcination temperatures of 200 °C, 400 °C, and 600 °C, respectively. Prior to characterization, all materials were thermally reduced in H$_2$ by heating at 2 °C/min to 250 °C. The Pd loading of the catalyst, 2.74 wt %, was determined by ICP-OES analysis. Analysis by X-ray diffraction (XRD, Figure 1a) confirmed that crystalline metallic Pd was formed under these conditions. The bare NbOPO$_4$ support exhibited reflections at 44.6°, 47.9°, and 57.6°, with an additional reflection arising at 39.8° after the addition and thermal reduction of Pd, corresponding to metallic Pd(111). No evidence of crystalline Pd oxide was observed. The Pd crystallite sizes were determined by XRD peak broadening by applying the Scherrer equation to the Pd(111) reflection (Table 1) and were found to increase from 4.7 to 8.2 to 15.2 nm with increasing calcination temperatures of 200, 400, and 600 °C, respectively. We note that metal nanoparticles sized below ~2 nm are not visible via XRD,[32] but we show (vide infra) that particles of this size, if existent, have negligible catalytic activity.

Table 1. Average Pd Particle Sizes (D) of Pd/NbOPO$_4$-200, 400, and 600 Were Measured by TEM (d_{TEM}) and Compared to Those Calculated by Applying the Scherrer Equation to Experimental XRD Patterns (d_{XRD})[a]

	d_{TEM} (nm)	d_{XRD} (nm)	Pd$_{\text{surf}}$ loading (μmol$_{\text{CO}}$/g$_{\text{cat}}$)	D (%)
Pd/NbOPO$_4$-200	3.0 ± 0.9	4.7	338.9	51
Pd/NbOPO$_4$-400	7.1 ± 2.5	8.2	203.2	31
Pd/NbOPO$_4$-600	23.6 ± 5.0	15.2	6.3	1

[a]CO chemisorption was used to probe the amount of surface Pd (Pd$_{\text{surf}}$) and calculate dispersion, the percentage of total Pd atoms exposed to the surface (D).

The Pd particle sizes were measured from transmission electron microscopy (TEM) images, representative versions of which are shown in Figure 1b and the corresponding particle diameter distributions in Figure 1c. The average particle sizes increased from 3.0 ± 0.9 to 7.1 ± 2.5 to 23.6 ± 5.0 nm with increasing calcination temperatures of 200, 400, and 600 °C, respectively. The Pd particle sizes determined by TEM image analysis agreed well with the crystallite sizes calculated from XRD peak broadening for the catalysts calcined at 200 and 400 °C. The Pd particle size was significantly larger than the crystallite size for the catalyst calcined at 600 °C, however, possibly due to polycrystallinity. Nonetheless, the notable increase in Pd crystallite sizes with calcination temperature, which is similar to size differences that lead to catalytic differences observed by Bethmont et al.[17] and Garcia-Ortiz et al.,[16] in addition to the narrow size distributions, indicates that the Pd/NbOPO$_4$ catalysts synthesized here are good model systems to investigate structure-performance trends in reductive etherification. The concentration of surface Pd (Pd$_{\text{surf}}$) was also obtained by CO chemisorption (Table 1). As expected, Pd$_{\text{surf}}$ loading, along with dispersion (D, Table 1) decreased with increasing pretreatment temperature and particle size.

Reductive etherification reactions were performed in a packed-bed reactor over the Pd/NbOPO$_4$ materials, and the effect of Pd particle size on the resulting rates and selectivity was evaluated between 16 and 26 h on stream. In agreement with the results of our previous work, little butanol or 4-heptanone conversion or reductive etherification selectivity was observed over the bare NbOPO$_4$ support (2.3% selectivity to 4-BH at 2% conversion). The reaction observed with the highest selectivity (92%) over NbOPO$_4$ was bimolecular dehydration of *n*-butanol to *n*-butyl ether, a reaction commonly observed over acidic oxides.[28,29] However, small amounts of 4-butoxyhept-3-ene (enol ether) were observed over the bare NbOPO$_4$ support (0.8% selectivity).

Based on the negligible reductive etherification rates over bare NbOPO$_4$, we confirmed that Pd particles are necessary to effectively catalyze reductive etherification. The effect of the Pd particle size on both selectivity and rate was evaluated by performing reductive etherification reactions over Pd/NbOPO$_4$-200, 400, and 600 at differential (6–15%) conversions. As previously observed[4] on Pd/NbOPO$_4$ (average particle size = 10 nm), we obtained ca. 80–83% selectivity to 4-butoxyheptane (4-BH) over all three Pd/NbOPO$_4$ materials (Figure 2a). The remaining 17–20% selectivity comprised of *n*-heptane, 4-heptanol, *n*-butyl ether, and 4-butoxyhept-3-ene (enol ether). These results indicate that the particle size does not have a significant effect on product selectivity.

Pd particle size did, however, dramatically influence the reductive etherification rates. The rate of reductive etherification over Pd/NbOPO$_4$-200 (d_{STEM} = 3.0 nm) was 53 μmol g$_{\text{cat}}^{-1}$ min^{-1}, and this quantity increased by 26% and 143% over

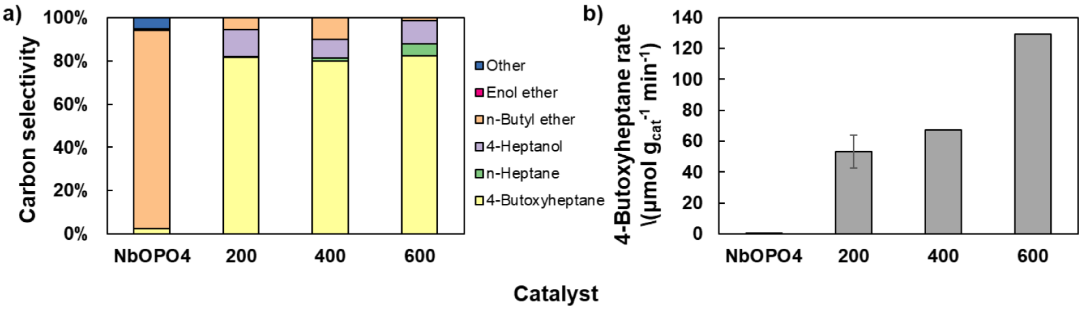

Figure 2. (a) Selectivity and (b) rates of reductive etherification over NbOPO$_4$ and Pd/NbOPO$_4$ materials (200: Pd/NbOPO$_4$-200, 400: Pd/NbOPO$_4$-400, 600: Pd/NbOPO$_4$-600) containing an increased particle size. Conditions: T = 200 °C, P_{Tot} = 70 bar, $PVP_{,n}$-butanol = 9.5 bar, $P_{\text{VP,4-heptanone}}$ = 6.1 bar, balance H$_2$, m_{Catalyst} = 0.20 g. Feed = 50 mol %/50 mol % 4-heptanone/n-butanol. WHSV = 13 g$_{\text{Feed}}$ g$_{\text{Catalyst}}^{-1}$ hr^{-1}. Species denoted "other" were detected and quantified in the GC FID but could not be precisely identified from the mass spectra. The error bar in the reductive etherification rate on the 200 °C heat-treated Pd/NbOPO$_4$ sample represents the standard deviation between measurements conducted over two catalyst loadings in two separate experiments.

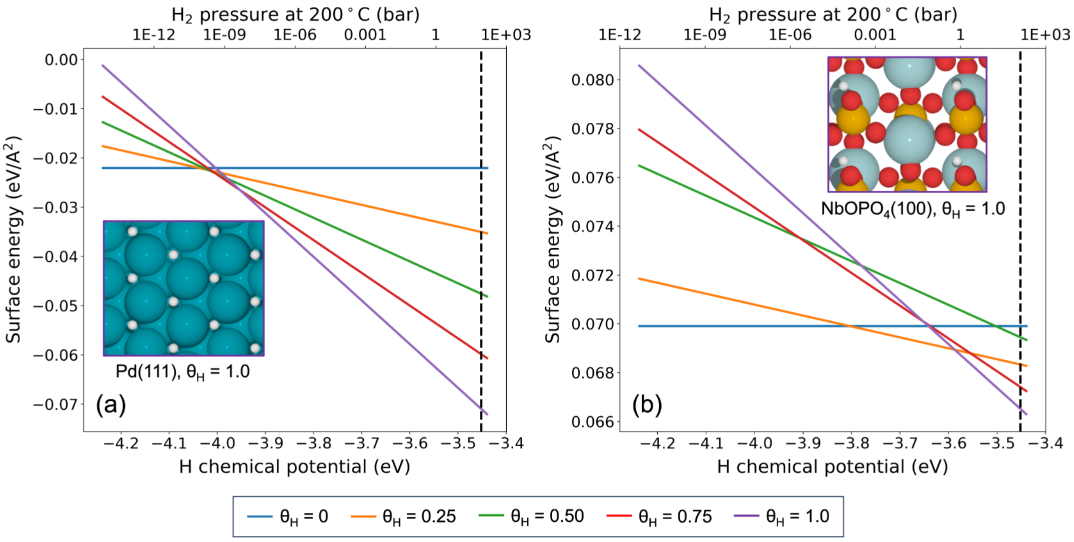

Figure 3. (a) Computed surface free energies of Pd(111) and (b) $NbOPO_4(100)$ at different surface coverages of H as a function of H chemical potential at T = 200 °C. The vertical black dashed lines indicate the hydrogen partial pressure used in the experiment, P_{H2} = 54.4 bar. Each inset shows the most stable surface coverage under the experimental conditions. Blue, light blue, white, red, and orange spheres represent Pd, Nb, H, O, and P atoms, respectively.

Scheme 1. Proposed Pathways for the Reductive Etherification Reaction[a]

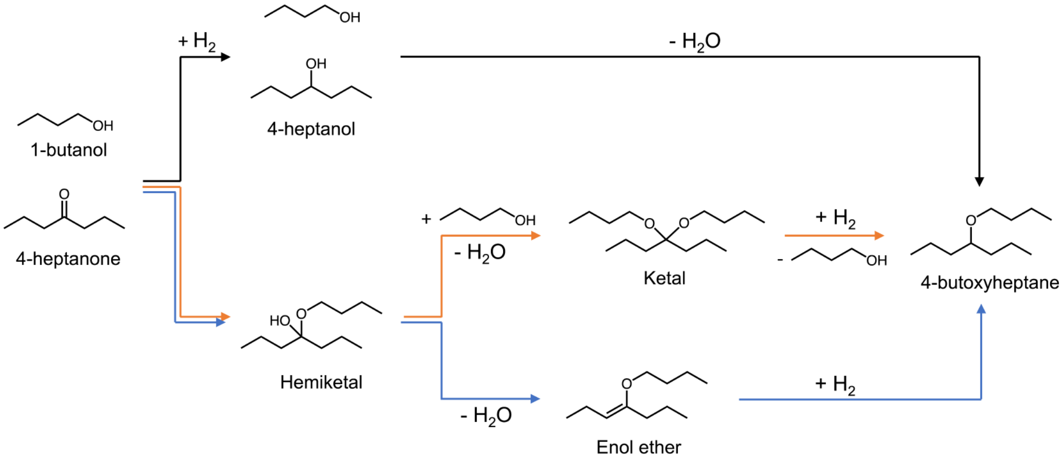

[a]Black, orange, and blue lines indicate the direct, ketal, and enol pathways, respectively.

$Pd/NbOPO_4$-400 and 600, respectively (Figure 2b). Thus, our findings of reductive etherification rates of 1-butanol and 4-heptanone increasing with Pd particle size over $Pd/NbOPO_4$ concur with those of Garcia-Ortiz et al.[16] and Bethmont et al.[17] in similar systems. These results suggest that specifically (i) both $NbOPO_4$ and Pd surfaces are necessary to facilitate reductive etherification and (ii) rates of reductive etherification are influenced by Pd particle size.

The experimental findings connecting Pd particle size to reaction rates also explain a trend in reductive etherification rates with time on stream observed over $Pd/NbOPO_4$-200. Figure S1 shows that etherification rates over this catalyst increase more than 3-fold from the earliest (2 h) to the latest (26 h) recorded times, such that rates over $Pd/NbOPO_4$-200 and 400 are nearly identical. We performed both pre- and postreaction catalyst characterization of $Pd/NbOPO_4$-200 by TEM ($Pd/NbOPO_4$-200 and $Pd/NbOPO_4$-200 spent, Figure 1a,b), which showed that the size of Pd particles increases from 3.0 ± 1.0 nm to 7.1 ± 3.5 nm; the latter size is identical to that of fresh $Pd/NbOPO_4$-400 within error (Table 1). Thus, the observed increase in the reductive etherification rate with time on stream over $Pd/NbOPO_4$-200 reflects Pd particle sintering, further substantiating the finding that reductive etherification rates increase with increasing Pd particle size. We note that the decrease in reductive etherification rate observed with time on stream over $Pd/NbOPO_4$-400 and 600 (Figure S1) is likely due to other phenomena outside the scope of this study (e.g., coking) and not Pd particle dispersion. The connection between the increased reductive etherification rate over time and Pd particle sintering observed over $Pd/NbOPO_4$-200 further exemplifies the experimental findings shown herein. Next, we will demonstrate the use of theoretical calculations to explain the role of the support and the catalyst particles in 4-BH formation and the impact of Pd particle size on reaction rates.

3.2. Density Functional Theory Study of Reductive Etherification.

3.2.1. Catalyst Models. We carried out DFT calculations to gain fundamental insights into the reaction mechanism of reductive etherification and substantiated the key findings presented in the Experimental section. To capture

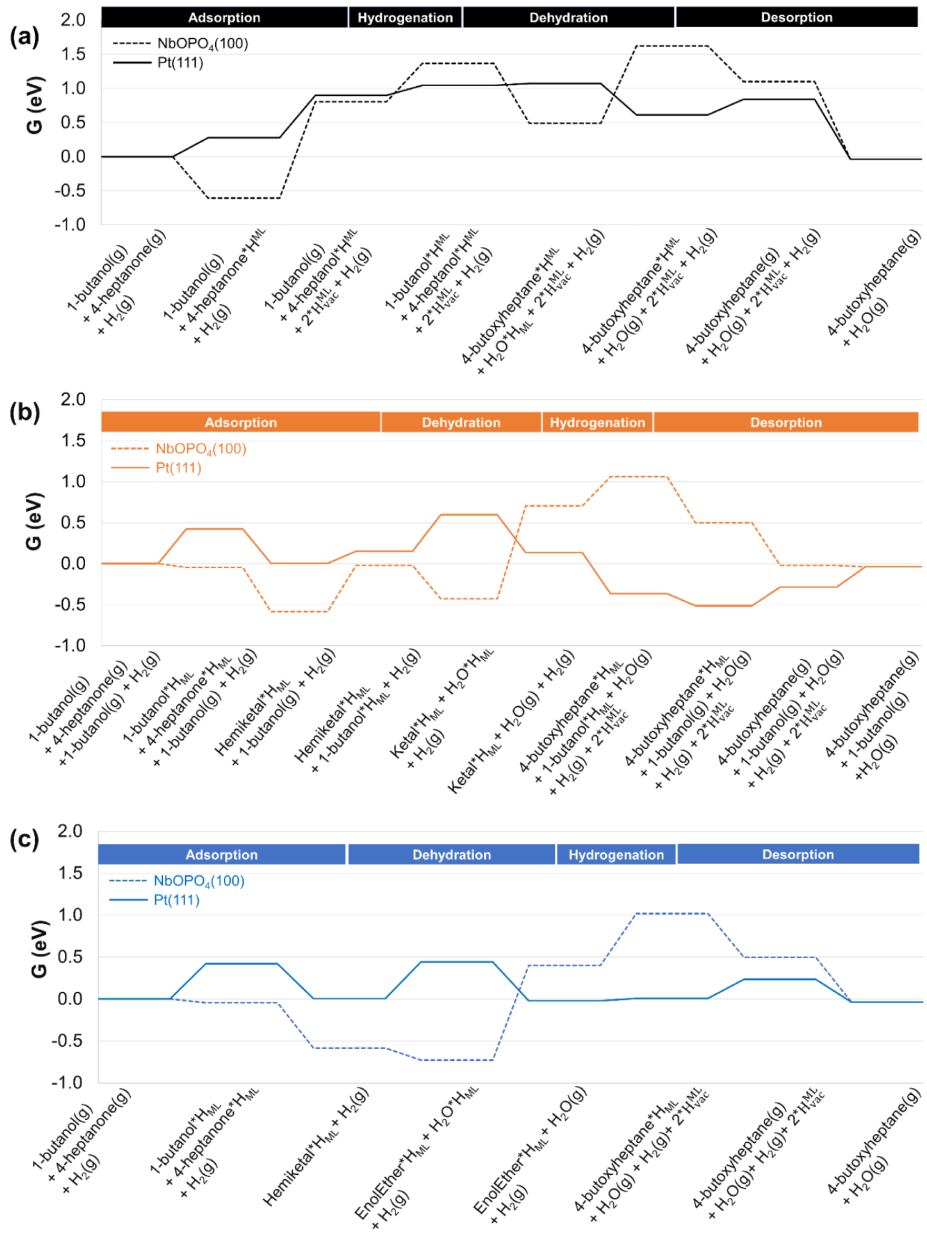

Figure 4. Potential energy surfaces of reductive etherification via the (a) direct, (b) ketal, and (c) enol pathways. $*H^{ML}$ and $*H^{ML}_{vac}$ represent an active site and a hydrogen vacancy, respectively, of the surfaces at 1 monolayer coverage of hydrogen.

the catalytic processes on the Pd/$NbOPO_4$ system, we modeled all reaction steps on both Pd and $NbOPO_4$ catalyst surfaces. Specifically, we chose the closest-packed Pd facet, Pd(111), and the well-ordered, flat $NbOPO_4$(100) as the representative surfaces for Pd and $NbOPO_4$ catalysts, respectively.[30,31] Furthermore, we performed surface free energy calculations to determine the optimal hydrogen coverages on both surfaces under the reaction conditions, i.e., T = 200 °C and P_{H2} = 54.4 bar. Figure 3 shows that a hydrogen coverage of 1 monolayer (θ_H = 1.0) is the most favorable on both Pd(111) and $NbOPO_4$(100). Hereafter, the Pd(111) and $NbOPO_4$(100) surfaces at 1 monolayer coverage of hydrogen will be employed as the catalyst models for Pd and $NbOPO_4$ in this work.

3.2.2. Reaction Mechanisms. Our DFT study considered three possible reductive etherification mechanisms: the direct, ketal, and enol pathways (Scheme 1).[4] In the direct pathway, 4-heptanone is reduced to 4-heptanol, and then the two alcohols couple to form 4-butoxyheptane. In contrast, the enol and ketal pathways both begin with the reaction between 1-butanol and 4-heptanone to form a hemiketal. From here, the two pathways diverge, with a second 1-butanol molecule coupling with the hemiketal in the ketal pathway and a dehydration of the hemiketal to an enol ether in the enol pathway.

We constructed potential energy surfaces (PESs) for the three considered pathways on both Pd(111) and $NbOPO_4$(100) surfaces based on the calculated free energies of relevant reaction intermediates, as shown in Scheme 1 (Figure 4). The adsorption geometries of surface intermediates can be found in Figure S2. Analysis of the PESs provides valuable insights into the mechanism of reductive etherification on Pd/$NbOPO_4$, particularly highlighting the most energetically favorable pathway. The high-energy barriers associated with the direct pathway (Figure 4a) due to the adsorption and hydrogenation of 4-heptanone to 4-heptanol on Pd(111) (1.04 eV) and $NbOPO_4$(100) (1.37 eV) render this route the least feasible. In contrast, the hemiketal and enol pathways present more favorable energetic profiles, suggesting their dominance in the reductive etherification process on Pd/$NbOPO_4$.

The ketal and enol pathways both begin with the same set of intermediates, as 1-butanol and 4-heptanone both adsorb to $NbOPO_4$(100) in a roughly energetically neutral step (−0.04 eV). Subsequently, the adsorbates combine to form an energetically favorable hemiketal intermediate (−0.54 eV). At this point, the two mechanisms diverge: the ketal pathway forms a ketal intermediate and a water molecule on $NbOPO_4$(100) after the adsorption of another 1-butanol molecule in a net-uphill step (0.16 eV), while the enol pathway dehydrates to form an enol ether over $NbOPO_4$(100) in a thermodynamically downhill step (−0.14 eV). For both pathways, the crossover between the energy profiles of $NbOPO_4$(100) and Pd(111), favoring the latter, indicates the possible diffusion of surface intermediates from $NbOPO_4$(100) to Pd(111). Hence, subsequent steps for both pathways are likely to occur on Pd(111) surfaces upon the desorption of water, an energetically uphill step that still leaves the enol pathway at a lower energy than the ketal pathway (−0.02 vs 0.14 eV). Subsequent hydrogenation steps (excluding product desorption) over Pd(111) are either thermoneutral or favorable in both pathways. The final step, which involves the regeneration of the hydrogenated Pd(111) surface, favors the enol (−0.24 eV) over the ketal pathway (0.28 eV). Thus, since the binding of the reactants and intermediates involved in the meaningful bond-breaking and bond-formation steps of the enol mechanism have the lowest Gibbs free energies, this mechanism is most likely responsible for reductive etherification. This conclusion aligns with our experimental observation of trace quantities of enol ether formation during reductive etherification (Figure 2a). Furthermore, Figure 4c demonstrates that the formation of enol ether is favorable on $NbOPO_4$, while hydrogenation predominantly occurs on Pd. These observations are consistent with the experimental observations.

The increase in 4-BH formation rates with increasing particle size of Pd, as shown in Figure 2b, suggests that the enol ether hydrogenation step, which primarily takes place on Pd, is kinetically relevant. Until now, our DFT analysis of reaction pathways included the implicit assumption that hydrogenation occurs on the Pd(111) facets of Pd nanoparticles. We performed nudged elastic band calculations and obtained the activation energies of enol ether hydrogenation on Pd(111), Pd(100), and Pd(110) to substantiate our assumption. The hydrogenation activation free energies are 0.35, 0.39, and 0.67 eV on Pd(111), Pd(100), and Pd(110), respectively. This finding suggests that the trend of facet catalytic activity follows Pd(111) > Pd(100) ≫ Pd(110) and justifies the use of the Pd(111) surface for modeling the hydrogenation of enol ether on Pd. In addition, the kinetic favorability of hydrogenation occurring on Pd(111) and Pd(100) over Pd(110) can also explain the trend of increasing reductive etherification activity with catalyst size, as shown in Figure 2b, as well as the observations of Garcia-Ortiz et al.[16] and Bethmont et al.[17] Since the enol ether to be hydrogenated is relatively large, with 11 carbon atoms, a substantial ensemble of Pd atoms is necessary to facilitate hydrogenation. As the Pd particle size increases, terrace sites like those on Pd(111) and Pd(100) will predominate over the step sites of Pd(110). Accordingly, a large, uninterrupted ensemble of Pd(111) atoms, free from step and other undercoordinated sites, is required for efficient reductive etherification; such ensembles will form more readily on larger Pd particles.

4. CONCLUSIONS

We demonstrate the reductive etherification of carboxylic acid-derived 4-heptanone and n-butanol to form 4-butoxyheptane over size-controlled Pd nanoparticles supported on $NbOPO_4$ in packed-bed reactor experiments and report two major findings. The first is that both catalyst functionalities ($NbOPO_4$ and Pd surfaces) are necessary for reductive etherification, and the second is that rates increase with increasing Pd crystallite size (5−15 nm). We employ density functional theory calculations to explain these findings and show that (i) the reaction occurs via the formation of an enol ether on the support surface and subsequent hydrogenation on Pd and (ii) hydrogenation rates are maximized over low-index metal surface facets like Pd(111). These findings provide a molecular-scale rationale for our experimental observations and can inform the development and scaling of processes to form low-carbon distillate fuels and other low-carbon-intensity chemicals via reductive etherification.

■ ASSOCIATED CONTENT

Supporting Information

The Supporting Information is available free of charge at https://pubs.acs.org/doi/10.1021/acsomega.4c09698.

Rates of reductive etherification over Pd/$NbOPO_4$ samples pretreated at varied temperatures and computed adsorption structures of reaction intermediates on $NbOPO_4$(100) and Pd(111) facets (PDF)

■ AUTHOR INFORMATION

Corresponding Authors

Rajeev S. Assary − *Materials Science Division, Argonne National Laboratory, Lemont, Illinois 60439, United States; Consortium for Computational Physics and Chemistry, Bioenergy Technologies Office, Washington, DC 20585, United States;* orcid.org/0000-0002-9571-3307; Email: jake.miller@lanzajet.com

Jacob H. Miller − *Catalytic Carbon Transformation & Scale Up Center, National Renewable Energy Laboratory, Golden, Colorado 80401, United States*; Email: assary@anl.gov

Authors

Hieu A. Doan − *Materials Science Division, Argonne National Laboratory, Lemont, Illinois 60439, United States; Consortium for Computational Physics and Chemistry, Bioenergy Technologies Office, Washington, DC 20585, United States*

Chenyang Li − *Materials Science Division, Argonne National Laboratory, Lemont, Illinois 60439, United States; Consortium for Computational Physics and Chemistry, Bioenergy Technologies Office, Washington, DC 20585, United States*

Nicole J. LiBretto − *Catalytic Carbon Transformation & Scale Up Center, National Renewable Energy Laboratory, Golden, Colorado 80401, United States;* Present Address: Honeywell UOP, Des Plaines, IL, 60016, United States

Alexander L. Rein – *Catalytic Carbon Transformation & Scale Up Center, National Renewable Energy Laboratory, Golden, Colorado 80401, United States*

Mingxia Zhou – *Materials Science Division, Argonne National Laboratory, Lemont, Illinois 60439, United States; Consortium for Computational Physics and Chemistry, Bioenergy Technologies Office, Washington, DC 20585, United States;* Present Address: College of Chemical Engineering and Environment, State Key Laboratory of Heavy Oil Processing, China University of Petroleum-Beijing, Beijing 102249, China

Glenn R. Hafenstine – *Catalytic Carbon Transformation & Scale Up Center, National Renewable Energy Laboratory, Golden, Colorado 80401, United States;* orcid.org/0000-0002-1294-7889

Derek R. Vardon – *Catalytic Carbon Transformation & Scale Up Center, National Renewable Energy Laboratory, Golden, Colorado 80401, United States*

Susan E. Habas – *Catalytic Carbon Transformation & Scale Up Center, National Renewable Energy Laboratory, Golden, Colorado 80401, United States;* orcid.org/0000-0002-3893-8454

Complete contact information is available at:
https://pubs.acs.org/10.1021/acsomega.4c09698

Author Contributions

$^{\nabla}$H.A.D. and C.L. contributed equally to this work. The manuscript was written through the contributions of all authors. All authors have given approval to the final version of the manuscript.

Notes

The authors declare no competing financial interest.

■ ACKNOWLEDGMENTS

This work was authored in part by the National Renewable Energy Laboratory, operated by Alliance for Sustainable Energy, LLC, and in part by Argonne National Laboratory, operated by UChicago Argonne, LLC, for the U.S. Department of Energy (DOE) under Contract Nos. DE-AC36-08GO28308 and DE-AC02-06CH11357, respectively. Funding was provided by the U.S. DOE Office of Energy Efficiency and Renewable Energy, Bioenergy Technologies Office. This research was conducted in collaboration with the Chemical Catalysis for Bioenergy (ChemCatBio) Consortium, a member of the Energy Materials Network (EMN), and the Consortium for Computational Physics and Chemistry (CCPC), funded by the Bioenergy Technologies Office (BETO). The views expressed in this article do not necessarily represent the views of the U.S. Department of Energy or the U.S. Government. The U.S. Government retains, and the publisher, by accepting the article for publication, acknowledges that the U.S. Government retains a nonexclusive, paid-up, irrevocable, worldwide license to publish or reproduce the published form of this work, or allow others to do so, for U.S. Government purposes.

■ REFERENCES

(1) Fairley, P. Introduction: Next Generation Biofuels. *Nature* **2011**, *474* (7352), S2–S5.

(2) Lynd, L. R.; Beckham, G. T.; Guss, A. M.; Jayakody, L. N.; Karp, E. M.; Maranas, C.; McCormick, R. L.; Amador-Noguez, D.; Bomble, Y. J.; Davison, B. H.; et al. Toward Low-Cost Biological and Hybrid Biological/Catalytic Conversion of Cellulosic Biomass to Fuels. *Energy Environ. Sci.* **2022**, *15* (3), 938–990.

(3) Huq, N. A.; Huo, X.; Hafenstine, G. R.; Tifft, S. M.; Stunkel, J.; Christensen, E. D.; Fioroni, G. M.; Fouts, L.; McCormick, R. L.; Cherry, P. A.; et al. Performance-Advantaged Ether Diesel Bioblendstock Production by a Priori Design. *Proc. Natl. Acad. Sci. U. S. A.* **2019**, *116* (52), 26421–26430.

(4) Hafenstine, G. R.; Huq, N. A.; Conklin, D. R.; Wiatrowski, M. R.; Huo, X.; Guo, Q.; Unocic, K. A.; Vardon, D. R. Single-Phase Catalysis for Reductive Etherification of Diesel Bioblendstocks. *Green Chem.* **2020**, *22* (14), 4463–4472.

(5) Kunkes, E. L.; Simonetti, D. A.; West, R. M.; Serrano-Ruiz, J. C.; Gärtner, C. A.; Dumesic, J. A. Catalytic Conversion of Biomass to Monofunctional Hydrocarbons and Targeted Liquid-Fuel Classes. *Science* **2008**, *322* (5900), 417–421.

(6) Yan, J.; Liang, L.; He, Q.; Li, C.; Xu, F.; Sun, J.; Goh, E.-B.; Konda, N. V. S. N. M.; Beller, H. R.; Simmons, B. A.; Pray, T. R.; Thompson, V. S.; Singh, S.; Sun, N. Methyl Ketones from Municipal Solid Waste Blends by One-Pot Ionic-Liquid Pretreatment, Saccharification, and Fermentation. *ChemSuschem* **2019**, *12* (18), 4313–4322.

(7) Huq, N. A.; Hafenstine, G. R.; Huo, X.; Nguyen, H.; Tifft, S. M.; Conklin, D. R.; Stück, D.; Stunkel, J.; Yang, Z.; Heyne, J. S.; et al. Toward Net-Zero Sustainable Aviation Fuel with Wet Waste–Derived Volatile Fatty Acids. *Proc. Natl. Acad. Sci. U. S. A.* **2021**, *118* (13), No. e2023008118.

(8) Pham, V.; Holtzapple, M.; El-Halwagi, M. Techno-Economic Analysis of Biomass to Fuel Conversion via the MixAlco Process. *J. Ind. Microbiol. Biotechnol.* **2010**, *37* (11), 1157–1168.

(9) Chan, W. N.; Fu, Z.; Holtzapple, M. T. Co-Digestion of Swine Manure and Corn Stover for Bioenergy Production in MixAlco$^{\mathrm{TM}}$ Consolidated Bioprocessing. *Biomass Bioenergy* **2011**, *35* (10), 4134–4144.

(10) Li, X.-L.; Zhang, K.; Chen, S.-Y.; Li, C.; Li, F.; Xu, H.-J.; Fu, Y. A Cobalt Catalyst for Reductive Etherification of 5-Hydroxymethyl-Furfural to 2,5-Bis(Methoxymethyl)Furan under Mild Conditions. *Green Chem.* **2018**, *20* (5), 1095–1105.

(11) Wei, J.; Wang, T.; Cao, X.; Liu, H.; Tang, X.; Sun, Y.; Zeng, X.; Lei, T.; Liu, S.; Lin, L. A Flexible Cu-Based Catalyst System for the Transformation of Fructose to Furanyl Ethers as Potential Bio-Fuels. *Appl. Catal., B* **2019**, *258*, 117793.

(12) Eagan, N. M.; Moore, B. M.; McClelland, D. J.; Wittrig, A. M.; Canales, E.; Lanci, M. P.; Huber, G. W. Catalytic Synthesis of Distillate-Range Ethers and Olefins from Ethanol through Guerbet Coupling and Etherification. *Green Chem.* **2019**, *21* (12), 3300–3318.

(13) Baddour, F. G.; Snowden-Swan, L.; Super, J. D.; Van Allsburg, K. M. Estimating Precommercial Heterogeneous Catalyst Price: A Simple Step-Based Method. *Org. Process Res. Dev.* **2018**, *22* (12), 1599–1605.

(14) Jadhav, D.; Grippo, A. M.; Shylesh, S.; Gokhale, A. A.; Redshaw, J.; Bell, A. T. Production of Biomass-Based Automotive Lubricants by Reductive Etherification. *ChemSuschem* **2017**, *10* (11), 2527–2533.

(15) Tulchinsky, M. L.; Briggs, J. R. One-Pot Synthesis of Alkyl 4-Alkoxypentanoates by Esterification and Reductive Etherification of Levulinic Acid in Alcoholic Solutions. *ACS Sustainable Chem. Eng.* **2016**, *4* (8), 4089–4093.

(16) Garcia-Ortiz, A.; Arias, K. S.; Climent, M. J.; Corma, A.; Iborra, S. Transforming Methyl Levulinate into Biosurfactants and Biolubricants by Chemoselective Reductive Etherification with Fatty Alcohols. *ChemSuschem* **2020**, *13* (4), 707–714.

(17) Bethmont, V.; Montassier, C.; Marecot, P. Ether Synthesis from Alcohol and Aldehyde in the Presence of Hydrogen and Palladium Deposited on Charcoal. *J. Mol. Catal. A: Chem.* **2000**, *152* (1), 133–140.

(18) Miller, J. T.; Schreier, M.; Kropf, A. J.; Regalbuto, J. R. A Fundamental Study of Platinum Tetraammine Impregnation of Silica: 2. The Effect of Method of Preparation, Loading, and Calcination

Temperature on (Reduced) Particle Size. *J. Catal.* **2004**, *225* (1), 203−212.

(19) Schneider, C. A.; Rasband, W. S.; Eliceiri, K. W. NIH Image to ImageJ: 25 Years of Image Analysis. *Nat. Methods* **2012**, *9* (7), 671−675.

(20) Kohn, W.; Sham, L. J. Self-Consistent Equations Including Exchange and Correlation Effects. *Phys. Rev.* **1965**, *140* (4A), A1133−A1138.

(21) Kresse, G.; Furthmüller, J. Efficient Iterative Schemes for Ab Initio Total-Energy Calculations Using a Plane-Wave Basis Set. *Phys. Rev. B* **1996**, *54* (16), 11169−11186.

(22) Blöchl, P. E. Projector Augmented-Wave Method. *Phys. Rev. B* **1994**, *50* (24), 17953−17979.

(23) Perdew, J. P.; Burke, K.; Ernzerhof, M. Generalized Gradient Approximation Made Simple. *Phys. Rev. Lett.* **1996**, *77* (18), 3865−3868.

(24) Grimme, S.; Antony, J.; Ehrlich, S.; Krieg, H. A Consistent and Accurate Ab Initio Parametrization of Density Functional Dispersion Correction (DFT-D) for the 94 Elements H-Pu. *J. Chem. Phys.* **2010**, *132* (15), 154104.

(25) Methfessel, M.; Paxton, A. T. High-Precision Sampling for Brillouin-Zone Integration in Metals. *Phys. Rev. B* **1989**, *40* (6), 3616−3621.

(26) Wisesa, P.; McGill, K. A.; Mueller, T. Efficient Generation of Generalized Monkhorst-Pack Grids through the Use of Informatics. *Phys. Rev. B* **2016**, *93* (15), 155109.

(27) Wang, Y.; Wisesa, P.; Balasubramanian, A.; Dwaraknath, S.; Mueller, T. Rapid Generation of Optimal Generalized Monkhorst-Pack Grids. *Comput. Mater. Sci.* **2021**, *187*, 110100.

(28) DeWilde, J. F.; Chiang, H.; Hickman, D. A.; Ho, C. R.; Bhan, A. Kinetics and Mechanism of Ethanol Dehydration on γ-Al 2O3: The Critical Role of Dimer Inhibition. *ACS Catal.* **2013**, *3* (4), 798−807.

(29) Kang, M.; Dewilde, J. F.; Bhan, A. Kinetics and Mechanism of Alcohol Dehydration on γ-Al2O3: Effects of Carbon Chain Length and Substitution. *ACS Catal.* **2015**, *5* (2), 602−612.

(30) He, J.; Tang, D.; Hu, C.; Luo, Y.; Kim, C. K.; Su, Z. Mechanistic Study on the Depolymerization of Typical Lignin-Derived Oligomers Catalyzed by Pd/NbOPO4. *Mol. Catal.* **2022**, *528*, 112500.

(31) Xia, Q.-N.; Cuan, Q.; Liu, X.-H.; Gong, X.-Q.; Lu, G.-Z.; Wang, Y.-Q. Pd/NbOPO4Multifunctional Catalyst for the Direct Production of Liquid Alkanes from Aldol Adducts of Furans. *Angew. Chem., Int. Ed.* **2014**, *53* (37), 9755−9760.

(32) O'Connell, K.; Regalbuto, J. R. High Sensitivity Silicon Slit Detectors for 1 nm Powder XRD Size Detection Limit. *Catal. Lett.* **2015**, *145*, 777−783.